The International Journal of Advanced Manufacturing Technology (2024) 134:751–763
https://doi.org/10.1007/s00170-024-14154-x

ORIGINAL ARTICLE

Application of the fracture-forming limit diagram for the analysis of cold formability of vanadium microalloyed steel 30MnVS6

André Rosiak[1] · Luana De Lucca de Costa[1] · Thomas Gomes dos Santos[1] · Lirio Schaeffer[1]

Received: 26 February 2024 / Accepted: 15 July 2024 / Published online: 25 July 2024

Abstract

This study investigates the cold formability of Vanadium microalloyed steel DIN 30MnVS6 by characterizing the material's mechanical behavior at room temperature and constructing the fracture-forming limit diagram. A carefully selected set of tests was conducted to establish formability limits in terms of local deformations. Concurrently, finite element numerical analysis was employed to deepen the understanding of the influence of local stress and strain states on the material's ability to deform without fracturing. The effects of geometric conditions, lubrication, and friction on formability were thoroughly investigated. Surface stress analysis highlighted the close relationship between formability and the stress state induced by process parameters. The construction of the fracture-forming limit diagram revealed that DIN 30MnVS6 exhibits formability comparable to steels widely used in cold forging. The steel proved to be a promising option for applications in this process, providing a viable alternative in terms of formability.

Keywords Cold forging · Formability · DIN 30MnVS6 · Fracture-forming limit diagram

1 Introduction

The global market for cold forged products was valued at \$11.63 billion in 2017, with a projected growth to reach \$17.25 billion by 2025 [1]. The continuous growth of this market is attributed to the fact that cold forging processes enable the manufacturing of components with complex geometries, excellent tolerances, and surface finish very close to the final form (near-net-shape). Cold work enhances the mechanical properties of the forged part, increasing mechanical strength, and microstructurally generating a grain-oriented structure in the direction of mechanical deformation. These effects allow the use of lower-cost materials as substitutes for steels with a higher percentage of alloying elements.

In the production of high-strength components, work hardening alone is insufficient to meet mechanical strength specifications, and post-forging heat treatments are necessary. Quenching, tempering, martempering, austempering, and surface treatments can be applied depending on the product requirements [2]. To reduce or even eliminate these heat treatments, several innovative approaches have been developed. One example is low-alloy boron steels. These materials exhibit good formability in the as-rolled state, eliminating the need for intermediate annealing due to low hardenability and forming martensite with an excellent hardness-to-toughness ratio, thus eliminating the need for tempering [3]. For the complete elimination of quenching and tempering heat treatments, cold forging of high-strength steels, such as bainitic [4], dual-phase, [5], TWIP [6], and TRIP [7] steels, has been the focus of studies. Despite the reduced ductility, which limits application to relatively simple geometries, these materials can exhibit yield strengths of up to 1600 MPa after cold forming [8], allowing for the suppression of subsequent heat treatments after forging.

In this context, there is an interest in the application of vanadium microalloyed steel DIN 30MnVS6 in cold forging. In this steel, the addition of a small amount of vanadium provides a distribution of fine carbonitride precipitates that ensure high mechanical strength in the as-rolled condition [9]. The high strength combined with work hardening generated during cold forming would be sufficient to meet strength requirements without the need for heat treatments.

In cold forging processes, plastic deformation and the forces required to generate strain are relatively high, leading

✉ André Rosiak
andre.rosiak@ufrgs.br

1 Metal Forming Innovation Center (CBCM), Federal University of Rio Grande Do Sul, Porto Alegre, Brazil

Table 1 Result of chemical analysis of DIN 30MnVS6 steel (% weight)

Element	C	Si	Mn	P	S	V
% weight	0,262	0,484	1,210	0,024	0,020	0,111

to a significant risk of material failure during processing. Thus, the applicability of a new material in cold forming depends on a comprehensive analysis of formability. As it is a high-strength steel, studying the formability of DIN 30MnVS6 steel is particularly relevant. Only through this investigation can defect-free production be achieved, avoiding high rates of raw material and energy wastage and ensuring the benefits of using this material in cold forging.

Formability analysis is conducted based on criteria derived from experimental studies related to industrial applications. In cold forging, formability limits are traditionally established in terms of the fracture-forming limit diagram (FFLD) [10–33].

Therefore, this work aims to analyze the cold formability of vanadium microalloyed steel DIN 30MnVS6, through the characterization of the material's mechanical behavior at room temperature and the establishment of DIN 30MnVS6 formability limits in terms of local strains, using the fracture-forming limit diagram. Additionally, numerical analysis using finite element methods is employed to enhance understanding of the effects of local stress and strain states on formability.

Table 2 Parameters of compression tests to survey the flow curve of DIN 30MnVS6

Sample diameter (mm)	8
Sample height (mm)	12
Roughness of compression dies (μm)	$R_a = 0.165$
Lubrication	PTFE
Equipment	EMIC universal testing machine with 600kN capacity
Tool speed (mm/s)	1

Table 3 Parameters used in the ring test

External diameter of samples (mm)	12
Inner diameter of samples (mm)	6
Sample height (mm)	4
Height reductions (%)	20
	40
	60
Lubrication	Zinc stearate
	Synthetic lubricant
	Without lubricant

2 Materials and methods

2.1 Initial characterization of DIN 30MnVS6

The DIN 30MnVS6 steel was provided by Gerdau® in the form of machine wire rods, approximately 500 mm in length and 16.15 mm in diameter. The steel underwent chemical analysis using a Q2ION spectrometer, BRUKER brand. The mass percentage results are listed in Table 1. The composition falls within the nominal range found in the literature [34].

Microstructural analysis of the material in its received condition was conducted through optical micrographs using conventional metallographic techniques. Image capture was performed on an inverted optical microscope, OLYMPUS brand, model GX-51. The average ferritic grain size was determined using the line intersection method, as described in ASTM E112, with the assistance of the ImageJ® software, which was also employed for determining the volumetric fraction of material microconstituents. Microhardness tests were carried out using a Microhardness Tester, model Hardness Tester ISH-TDV 1000, INSIDE brand. Three samples were tested, and the average of 10 measurements on each sample was established as the Vickers hardness in the initial condition.

2.2 Mechanical behavior characterization of DIN 30MnVS6

There is a lack of consistent information in the literature regarding the mechanical behavior of DIN 30MnVS6 during cold forming. Therefore, mechanical tests were conducted to analyze how the steel responds to plastic deformation at room temperature. In this stage, uniaxial compression tests were performed to generate the flow curve. Additionally, the ring test was included in this phase to determine the coefficient of friction under the lubrication conditions used in subsequent tests. The details of the compression tests for generating the flow curve are listed in Table 2.

Friction between the samples and the flat dies used in the compression tests was quantified through the ring test [35]. Table 3 outlines the parameters of the tests conducted to define the coefficient of friction (μ). Calibration curves for the ring test on DIN 30MnVS6 steel were obtained through finite element analysis. Two-dimensional numerical simulations were performed using Simufact.Forming® 15.0 software, with the samples discretized into triangular elements with a size of 0.3 mm.

2.3 Construction of the fracture-forming limit diagram of DIN 30MnVS6

The FFLD is derived from compression tests on cylindrical specimens. During compression, the expanding lateral surface of the cylinder takes on a barrel shape, and fracture on the free surface occurs, initiating at the midpoint. To define the material's formability limit, the conventional cylindrical coordinate system (r, θ, z) is assumed, and the strain components of the external surface of the cylinder are calculated. Circumferential (φ_θ) and axial (φ_z) strains that develop at the midpoint of the sample are calculated from the beginning of compression until the moment fracture is observed. The evolution of deformations during compression is referred to as the deformation path. Connecting the endpoints of the deformation paths, corresponding to the values of φ_θ and φ_z at the moment of fracture, generates the fracture-forming limit line.

Compression tests to define the formability limit of DIN 30MnVS6 were carried out in different geometries and friction conditions, allowing a broad assessment of the influence of stress and deformation states on the occurrence of fracture. Figure 1 lists the test conditions, geometries, and dimensions of compression samples.

In compression tests, the moment of fracture is determined by observing the initiation of cracks in the mid-area of the external surface of the samples. However, to enhance the precision of fracture detection, the following methodology was followed:

- Preliminary tests were conducted for all sample conditions to determine the approximate fracture height. In these tests, the samples underwent height reduction increments of 0.5 until cracks were observed.
- New tests were carried out with the samples initially subjected to a height reduction 10% less than that defined in the preliminary tests. Subsequently, height reduction increments of 2.5% were performed, followed by inspection under an optical microscope with a 50 × magnification. This testing method ensures that the measurement error is within 2.5% of the initial sample height.

For the calculation of surface axial strains, a grid of circles with a diameter of 2.3 mm was electrochemically marked on the samples. Figure 2 shows the cylindrical sample positioned between the flat dies (Fig. 2a) and highlights the grid marked on the surface of the sample (Fig. 2b).

Axial strains were calculated based on the variation in the dimensions of the circle marked on the lateral center of the samples. After each deformation increment, the grid was measured using an optical microscope with a 50 × magnification. Circumferential strains were calculated from the variation in the equatorial diameter of the samples, measured with a caliper after each deformation increment.

	Geometry	Sample	h_0	d_0	h_b	d_b	Lubrication		Geometry	Sample	h_0	d_0	h_b	d_b	Lubrication
1	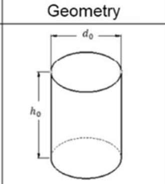	Cylindrical $\frac{h_0}{d_0} = 1{,}5$	12	8	-	-	Zinc Stearate	5	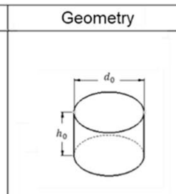	Cylindrical $\frac{h_0}{d_0} = 0{,}75$	6	8	-	-	Without lubricant
2	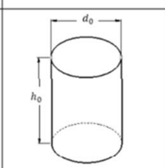	Cylindrical $\frac{h_0}{d_0} = 1{,}5$	12	8	-	-	Synthetic lubricant	6	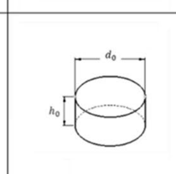	Cylindrical $\frac{h_0}{d_0} = 0{,}5$	4	8	-	-	Without lubricant
3	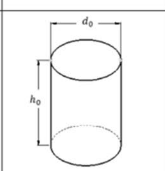	Cylindrical $\frac{h_0}{d_0} = 1{,}5$	12	8	-	-	Without lubricant	7	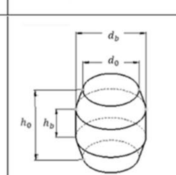	Conical	8	6,4	4	8	Without lubricant
4	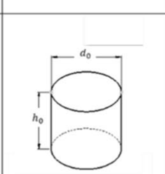	Cylindrical $\frac{h_0}{d_0} = 1{,}0$	8	8	-	-	Without lubricant	8	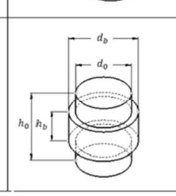	Flanged	8	6,4	4	8	Without lubricant

Fig. 1 Test conditions, geometries, and dimensions of compression samples

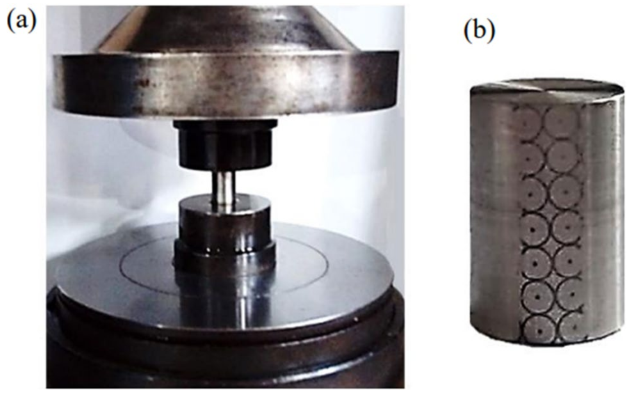

Fig. 2 **a** Cylindrical sample with positioned between the flat plates and **b** grid of circles marked on the surface of the sample

The measurement of the grid dimensions and sample inspection was carried out using an OLYMPUS DP-GX-51 inverted microscope through the AnalySIS® image capture software. Figure 3 shows the variation of the grid dimensions on the surface of the samples during the compression tests and the detection of the fracture using an optical microscope.

Numerical simulations of all tests were performed to construct the deformation diagram. 2D numerical simulations were conducted using the Simufact.Forming® 15.0 software, with samples discretized into triangular elements with a size of 0.3 mm.

3 Results and discussions

3.1 Initial characterization of DIN 30MnVS6

The microstructure of DIN 30MnVS6 steel in the as-received condition is depicted in Fig. 4.

The microstructure comprises proeutectoid ferrite and pearlite. The volumetric fraction of pearlite is 38.1%, while the remaining 61.9% corresponds to ferrite. The ferritic grains are equiaxial with an average size of 5 µm. The refined microstructure and the volumetric fraction of the pearlite observed in Fig. 4 contribute to the material's hardness. Microhardness profiles indicate values ranging from 290 to 312 HV, with an average of 295 HV.

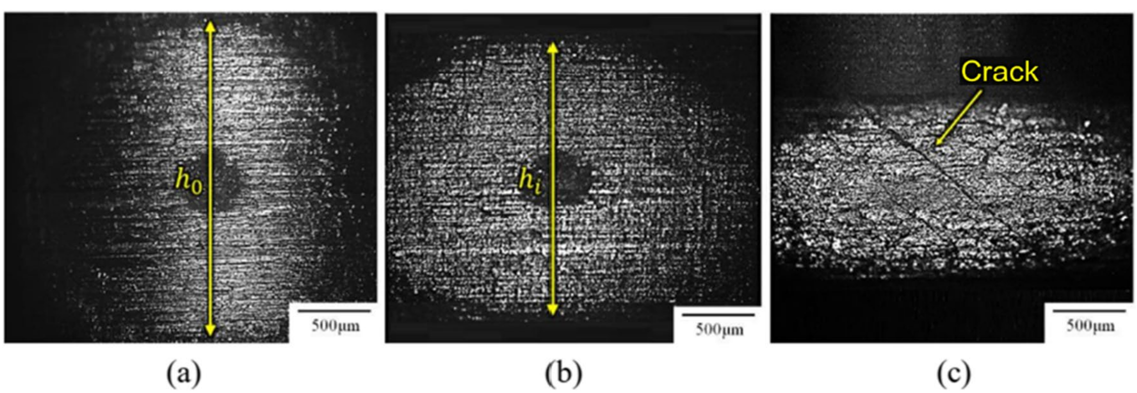

Fig. 3 Inspection and measurement of the grid mark on the surface of the samples. **a** Sample before the start of compression, **b** after deformation increments, and **c** at the moment of fracture detection

Fig. 4 Micrographs of DIN 30MnVS6 in the condition received with magnification of **a** 1000× and **b** 500× (nital 2%)

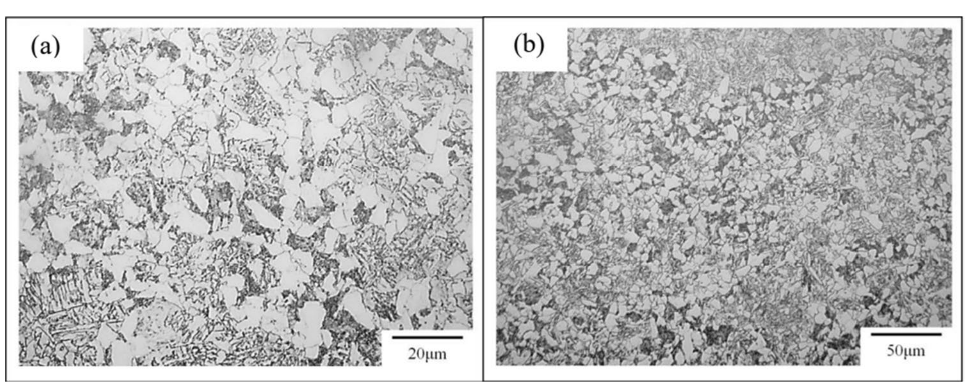

3.2 Flow curve of DIN 30MnVS6

Understanding the material's flow curve is essential in any mechanical forming process. The flow curve obtained from room temperature compression tests for DIN 30MnVS6 steel is shown in Fig. 5.

From the experimental data, the Hollomon equation describing the mechanical behavior of the material when cold-deformed was defined. The Hollomon equation for the microalloyed steel DIN 30MnVS6 is expressed as follows:

$$k_f = 1397.6\ \varphi^{0.13} \tag{1}$$

Equation 1 was implemented in the simulation software Simufact Forming 15.0 for numerical analyses.

3.3 Friction analysis

The calibration curves of the ring test for DIN 30MnVS6 steel, obtained through finite element analysis, are shown in Fig. 6. The curves include adjusted experimental values for the three friction conditions employed in the compression tests conducted in this study.

The application of zinc stearate on the contact interfaces proved to be the best lubrication condition, with a coefficient of friction equal to 0.05. The use of synthetic lubricant resulted in a friction coefficient of 0.09. When no lubrication was applied, the friction coefficient was 0.15.

Friction plays a crucial role in conducting compression tests to determine the formability diagram, intensifying circumferential tensile stresses that lead to surface fracture [10]. To ensure the numerical results are employed in a precise analysis of experimental tests, the friction coefficient values used in simulations must reliably quantify the real condition. To guarantee the accuracy of numerical results, two forms of validation were performed. First, the force–displacement curves from the experimental procedure were compared to those obtained through numerical simulations. Then, a comparison was made between the maximum diameter value of the sample (at mid-height) obtained experimentally and numerically at the end of the process [36]. Figure 7 illustrates how the measurement is conducted.

The numerical results demonstrated that the friction coefficient values, defined by the ring test, were able to reflect the real condition in compression tests with cylindrical samples. However, in the compression of conical and flanged samples, numerical and experimental results diverged considerably. Thus, to define the friction conditions developed during the compression of pre-bulged samples, an inverse analysis of the process was employed. The correct value of the friction coefficient was found iteratively through numerical simulations of the tests. The inverse analysis of the tests, by trial and error, was conducted until the numerical results matched those obtained experimentally. It was verified that for pre-bulged samples, friction is higher. In these samples, the unlubricated condition generated a friction coefficient of 0.18. These results are in accordance with the literature [37], which shows that more severe friction conditions are found in non-cylindrical samples, i.e., with pre-bulging geometry.

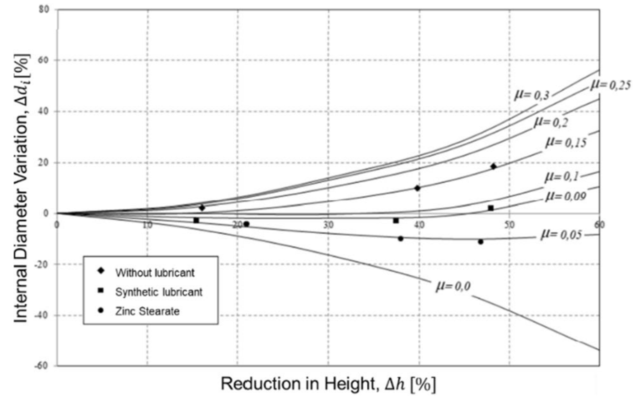

Fig. 6 Ring test calibration curves for DIN 30MnVS6 steel

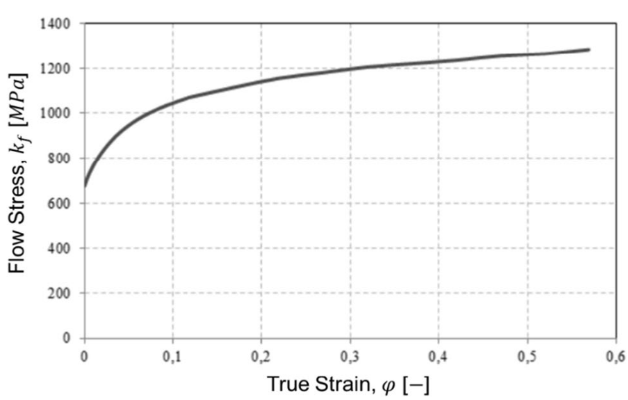

Fig. 5 Flow curve of DIN 30MnVS6 steel obtained by the compression test

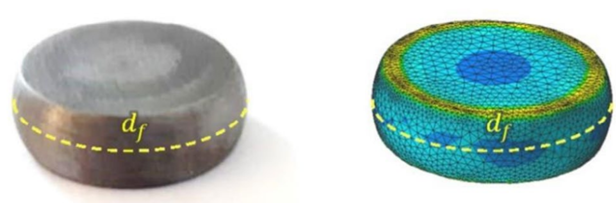

Fig. 7 Comparison between the maximum diameter of the sample after the test and the numerical simulation

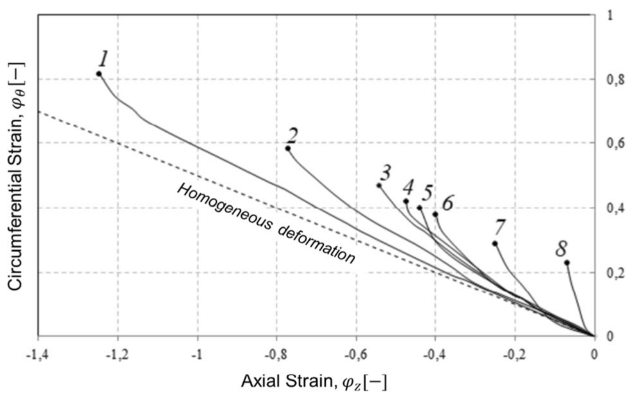

Fig. 8 Deformation trajectories obtained for DIN 30MnVS6 microalloyed steel

3.4 Deformation paths

Assuming the conventional cylindrical coordinate system, the deformation components on the free surfaces of compressed samples consist of circumferential deformations φ_θ (tensile) and axial deformations φ_z (compressive). Experimentally determined deformation paths for DIN 30MnVS6 steel are shown in terms of the principal surface deformations in Fig. 8.

These deformation paths represent the variations of circumferential deformations (φ_θ) as a function of axial deformations (φ_z) during the compression test. These paths are crucial for understanding the material's behavior during plastic deformation, serving as an essential tool in formability analysis. In Fig. 8, it can be observed how the deformation paths for DIN 30MnVS6 steel were experimentally delineated, providing crucial insights into the material's behavior under compressive loads.

These paths are valuable for constructing the fracture-forming limit diagram, offering insights into safe processing conditions, and aiding in the assessment of surface fracture during the cold forming process.

The relationship between the principal strain and, consequently, the behavior of the deformation paths obtained in the compression tests is affected by friction and the initial geometry of the samples [38]. The selected set of conditions for the tests allowed for a wide range of relationships between circumferential and axial strain at fracture to be obtained. Between the flanged sample, with the lowest magnitude of φ_θ and φ_z at fracture, and the cylindrical sample with zinc stearate lubrication, the condition with the highest magnitude of φ_θ and φ_z at fracture, axial strain varied between − 0.07 and − 1.24, while circumferential strain ranged from 0.22 to 0.81. This dispersion of results not only enables the determination of the forming limit line but also ensures greater reliability of the results.

Despite the distinct behavior of the deformation paths, some similarities can be highlighted. All deformation trajectories exhibit non-linearity from the beginning to fracture. Furthermore, the slope of the deformation paths increases as the measurement point approaches the fracture point. This means that at the moment of fracture, the increment of axial strain is almost zero, while the increment of circumferential strain is high [39].

For a better understanding of how friction conditions and sample geometry influence the relationship between φ_θ and φ_z, the deformation paths presented in Fig. 8 were divided into three groups, varying friction, the ratio between height and initial diameter (h_0/d_0) of cylindrical samples, and the geometry of the samples through pre-buckling by machining.

3.4.1 Friction effect

Figure 9 shows how variations in friction conditions affect the deformation paths of DIN 30MnVS6 steel. The geometry of samples 1, 2, and 3 is identical, and the change in results is solely due to the modification of the lubrication condition. The deformation path for frictionless compression, called homogeneous deformation, is also shown. In homogeneous deformation, the absence of friction prevents the barrel distortion of the cylinder from developing, and thus, surface stresses are uniform. Theoretically, in this condition, crack mechanisms cannot occur, and tensile deformation is equal to half of the compressive deformation along the entire deformation path, generating a constant slope of − 0.5. Due to friction, the experimentally determined deformation paths deviated from the slope of homogeneous deformation.

Samples 1, 2, and 3, due to the different lubrication conditions used, had coefficients of friction of 0.05, 0.09, and 1.5, respectively. In compression with a higher coefficient of friction (sample 3), the slope of the deformation path is greater, and the relationship between φ_θ and φ_z capable of causing fracture is reached more quickly.

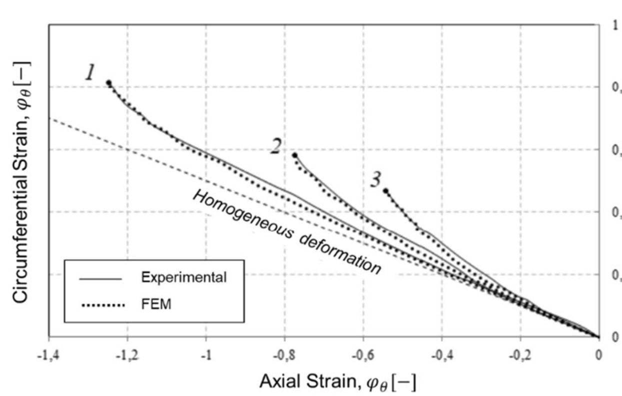

Fig. 9 Effect of varying friction conditions on the deformation trajectories of DIN 30MnVS6 microalloyed steel

With the reduction of the friction coefficient, the slope of the deformation paths becomes smoother. For a sample with $\mu = 0.05$, the path becomes almost linear, approaching homogeneous deformation. Thus, with reduced friction, the magnitude of surface deformations at fracture is increased. Better lubrication conditions reduce the barrel distortion of the cylinder and, consequently, the magnitude of surface tensile stresses in the circumferential direction. Thus, the degree of deformation achieved before fracture is significantly increased. In tests where zinc stearate was used as a lubricant, a reduction in height at fracture of 80.8% was obtained, while for the non-lubricated condition, this value was 57.6%.

3.4.2 Effect of initial cylinder dimensions

Figure 10 shows the effect of the ratio between the height and initial diameter (h_0/d_0) of cylindrical samples on the deformation paths. The friction condition of the tests for samples 3, 4, 5, and 6 was the same so that only the effect of changing the initial dimensions could be observed. The uneven distribution of deformation along the material generated by friction during compression is amplified as the h_0/d_0 ratio is reduced. As a result, the barrel distortion of the sample is accentuated, tilting the deformation path upwards. Thus, as the h_0/d_0 ratio of the samples was reduced from 1.5 to 0.5, the magnitude of deformations at fracture was also reduced.

3.4.3 Effect of pre-barreling of samples

Figure 11 illustrates the effect of varying the geometry of samples through machining pre-barreling on the deformation paths. The results of conical and flanged samples are compared to the result of the cylindrical sample, with the same friction condition maintained in all tests.

Pre-barreling of the samples, with the machining of conical and flanged shapes, allows the effects discussed earlier to be combined. The conical and flanged geometries simulate the effect of reducing h_0/d_0 and amplify the friction effect,

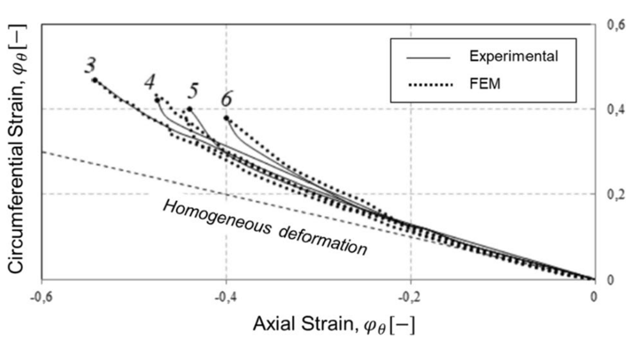

Fig. 10 Effect of varying the h_0/d_0 ratio of cylindrical samples on the deformation trajectories of DIN 30MnVS6 microalloyed steel

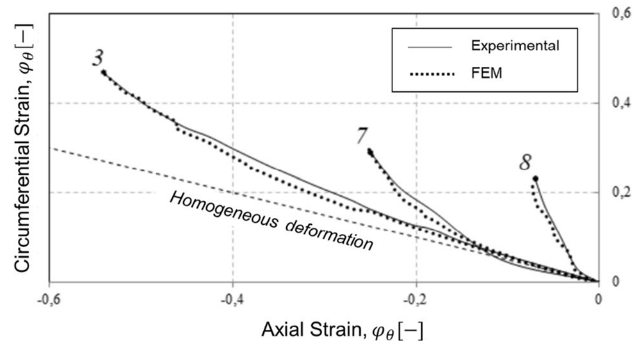

Fig. 11 Effect of sample pre-stacking on the deformation trajectories of DIN 30MnVS6 microalloyed steel

even generating an increase in the coefficient of friction. As a result, the deformation paths of these samples show a more significant increase in slope. The flanged geometry exhibits the deformation path with the highest slope among the tested samples. This behavior is very similar to that found in axial tension tests since the sample's surface is subjected to high circumferential stress from the beginning [40]. The smoother slope of the deformation path of the conical sample resembles an intermediate behavior between tension and compression tests [37].

In Figs. 9, 10, and 11, in addition to the experimentally obtained deformation paths (solid lines), the evolutions of surface deformations obtained by numerical simulation (dashed lines) are shown. Numerical results agree with experimental ones along all deformation paths, with differences not exceeding 5% at any point. It is believed that the relatively small differences between finite element calculations and experimental results are likely caused by simplifications made in the simulation process. In simulations, the friction coefficient is defined as constant during the test. Possible variations in the actual value of the friction coefficient during plastic deformation can generate a noticeable difference in numerical results. Additionally, in simulations, the material is considered isotropic and homogeneous, and any material detail affecting experimental results is not considered in the numerical calculations [40].

3.5 Analysis of surface stress

The deformation paths obtained in compression tests also allow for the analysis of surface stresses developed in the samples, thus providing an understanding of the stress state at fracture. The stress components are calculated from the Levy–Mises equations that relate increments of plastic deformation to the stress of an isotropic material, expressed in cylindrical coordinates as [10]:

$$d\varphi_r = d\lambda[\sigma_r - (\sigma_\theta + \sigma_z)/2] \tag{2}$$

$$d\varphi_\theta = d\lambda[\sigma_\theta - (\sigma_r + \sigma_z)/2] \tag{3}$$

$$d\varphi_z = d\lambda[\sigma_z - (\sigma_\theta + \sigma_r)/2] \tag{4}$$

The increment of equivalent deformation ($d\varphi_{eq}$) and the equivalent stress (σ_{eq}) are expressed as:

$$d\varphi_{eq} = \frac{\sqrt{2}}{3}[\left(d\varphi_r - d\varphi_z\right)^2 + \left(d\varphi_z - d\varphi_\theta\right)^2 + (d\varphi_\theta - d\varphi_r)^2]^{1/2} \tag{5}$$

$$\sigma_{eq} = \frac{1}{\sqrt{2}}[\left(\sigma_r - \sigma_z\right)^2 + \left(\sigma_z - \sigma_\theta\right)^2 + (\sigma_\theta - \sigma_r)^2]^{1/2} \tag{6}$$

where $d\varphi_r$, $d\varphi_\theta$, and $d\varphi_z$ are the incremental deformations, and σ_r, σ_θ, and σ_z are the stresses in the $\overline{r}$, $\overline{\theta}$, and $\overline{z}$ directions. $d\lambda$ is a proportionality constant that depends on the material and the level of deformation given by $d\varphi_{eq}/\sigma_{eq}$. For the considered surface area, the stress in the r direction is zero, and the stress state becomes planar. By modifying Eqs. 4 and 5, the stress components on the surface of the samples during compression can be calculated according to the following equations:

$$\sigma_z = \frac{\sigma_{eq}}{\sqrt{3}}\left(\frac{2\alpha + 1}{\sqrt{\alpha^2 + \alpha + 1}}\right) \tag{7}$$

$$\sigma_\theta = \frac{\sigma_{eq}}{\sqrt{3}}\left(\frac{\alpha + 2}{\sqrt{\alpha^2 + \alpha + 1}}\right) \tag{8}$$

where α is the slope of the deformation paths calculated during the compression test, given by $\alpha = d\varphi_z/d\varphi_\theta$. The equivalent stress σ_{eq} is obtained from the material's flow curve, defined by a uniaxial compression test.

The deformation paths shown in Fig. 8 were approximated by third degree polynomials, and the equations that describe the variation of φ_θ as a function of φ_z are listed in Table 4. Knowledge of the experimental history of plastic deformations, expressed by the equations in Table 4, allows the evaluation of the evolution of surface stress components as a function of equivalent strain (φ_{eq}) as shown in Fig. 12. The solid lines correspond to the values obtained experimentally, calculated using Eqs. 7 and 8, while the dotted lines refer to the results obtained via numerical simulation. The radial stress gradient (σ_r) is negligible in the equatorial region of the cylinder; therefore, in this region, the stress state is essentially plane stress. Furthermore, the shear stress and strain components are zero due to symmetry. The stress state in the equatorial region of the external surface of the samples is then formed by the axial (σ_z) and circumferential (σ_θ) stresses [36].

Table 4 Equations that describe the deformation trajectories

Sample	Equation	R^2
1	$\varphi_\theta = -0.0488\varphi_z^3 + 0.0158\varphi_z^2 - 0.5359\varphi_z - 0.0024$	0.9989
2	$\varphi_\theta = -0.507\varphi_z^3 + 0.1953\varphi_z^2 - 0.5892\varphi_z - 0.0024$	0.9999
3	$\varphi_\theta = -0.8696\varphi_z^3 + 0.0204\varphi_z^2 - 0.6125\varphi_z - 0.001$	0.9993
4	$\varphi_\theta = -0.7714\varphi_z^3 + 0.283\varphi_z^2 - 0.5529\varphi_z - 0.0003$	0.9975
5	$\varphi_\theta = -4.2764\varphi_z^3 - 1.6493\varphi_z^2 - 0.735\varphi_z - 0.0091$	0.9933
6	$\varphi_\theta = -6.6398\varphi_z^3 - 2.4695\varphi_z^2 - 0.8547\varphi_z - 0.0009$	0.9974
7	$\varphi_\theta = -1.8517\varphi_z^3 + 5.3086\varphi_z^2 - 0.0619\varphi_z - 0.0002$	0.9975
8	$\varphi_\theta = 326.8\varphi_z^3 + 71.672\varphi_z^2 + 0.1621\varphi_z - 0.0003$	0.9984

Analyzing Fig. 12, it is possible to verify that, for all test conditions, as the equivalent strain advances, the modulus of tensile stresses increases, while that of compressive stress decreases. Consequently, the hydrostatic stress component $\sigma_m = (\sigma_1 + \sigma_2 + \sigma_3)/3$ becomes increasingly tensile, generating a high fracture tendency [41]. Despite the seemingly similar behavior of stress components, the level of equivalent strain reached before fracture varied considerably. Sample 1 achieved the best result, reaching an equivalent strain close to 1.3 before fracture, while sample 8, with the worst result, did not exceed an equivalent strain of 0.17. The significant variation in strain at fracture among the tested samples is associated with the test conditions. Comparing the behavior of the sample deformed under the best conditions, sample 1, and the specimen subjected to the most severe conditions, sample 8, allows a better understanding of how geometric and friction conditions affect the local stress state of the samples and, consequently, formability.

In the compression of sample 1, due to good lubrication, the axial stress gradually increases during height reduction. Throughout most of the test, the average stress is compressive. Thus, only at the end of compression do tensile stresses predominate on the material's surface, allowing higher levels of equivalent strain to be achieved before fracture. In sample 8, on the other hand, the flanged geometry and high friction make the stress state tensile from the beginning of compression, with high circumferential stresses and low axial stresses. The severe bulging of the sample is so pronounced that the initially compressive axial stress becomes tensile at the end of the process. As a result, the stress state that produces the conditions for crack nucleation is reached more quickly, leading to premature sample fracture.

It is important to note the effect of lubrication on the magnitude of tensile stresses. In samples 1 and 2, lubricating the contact interfaces between the parts and the tools significantly reduced the intensity of circumferential stresses on the surface of the samples. With reduced friction, the bulging of

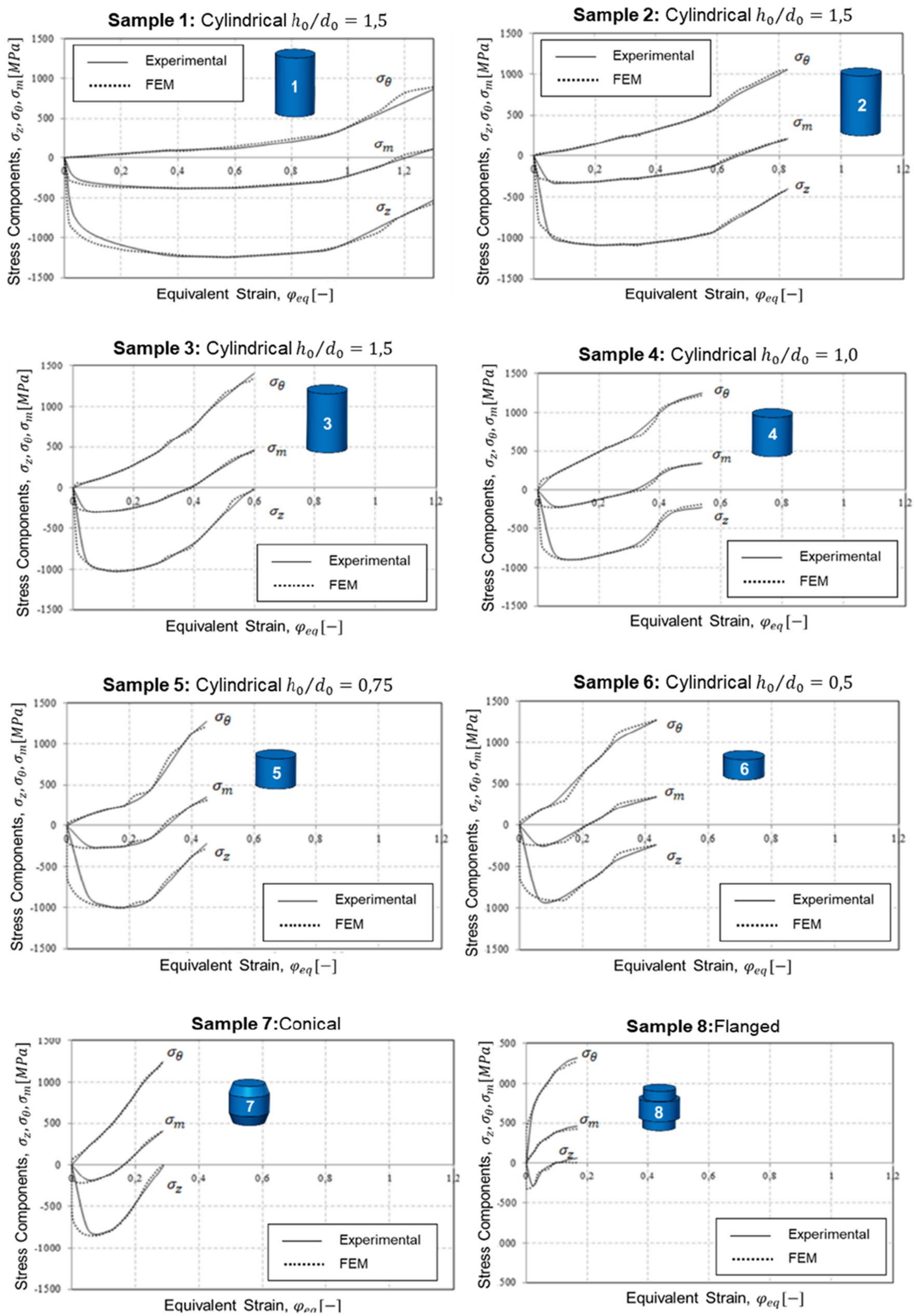

Fig. 12 Evolution of the circumferential (σ_θ), longitudinal (σ_z), and hydrostatic (σ_m) stress components as a function of equivalent strain (φ_{eq}), during compression tests

the samples is also reduced, making tensile stresses milder. The maximum values of circumferential stresses for non-lubricated samples practically did not vary, being close to 1300 MPa for all geometries (samples 3 to 8). However, the use of zinc stearate lubrication (sample 1) resulted in a reduction of this value by approximately 33%, while the use of synthetic lubricant (sample 2) reduced the maximum tensile stress on the surface of the samples by almost 20%.

It is clear that increasing friction; reducing the h_0/d_0 ratio; and, especially, pre-bulging the samples accelerate the change in stress state from compressive to tensile, and thus, the occurrence of fracture. The stress state induced by process parameters significantly influences the opening or closing of small cracks and can limit or accelerate their growth. Due to this important role of stress state, it is not possible to express formability solely in terms of material. Formability also depends on process variables such as strain, strain rate, and temperature [10]. The tests conducted in this study were performed at low speeds, so the effect of temperature and strain rate can be neglected. However, in industrial practice, deformation speeds often exceed 50 s^{-1}, potentially generating a temperature increase in the working material of up to 350 °C [2]. In these cases, the effect of temperature and deformation rate must be controlled during the process.

These results demonstrate that in compression forming, significantly higher degrees of strain can be achieved compared to processes dominated by tensile stress. In other words, for a given material, temperature, and strain rate, the higher the compressive hydrostatic stress, the better the material's formability.

The correlation between numerical and experimental results shown in Fig. 12 was good, allowing for an expanded analysis of stresses through numerical simulations. Figure 13 shows the distribution of hydrostatic stresses in the longitudinal sections of the cylindrical sample with $\frac{h_0}{d_0} = 1.5$ (sample 1) and the conical sample (sample 7) until the moment of fracture. Due to excellent lubrication conditions, the stress state in the cylindrical sample is predominantly compressive until the penultimate stage recorded in Fig. 13. The bulging of the sample only develops, altering the stress state, when the sample height becomes very small compared to the diameter. From this moment on, the bulging of the sample intensifies, altering the hydrostatic stress on the surface, while the rest of the volume has its stress state practically unchanged. The change in the superficial stress state, with the intensification of tensile stresses, quickly leads to fracture in this region.

In the conical sample, due to the bulging, the average surface stress becomes positive prematurely. With the rapid predominance of the tensile stress state, the remaining compression results only in the concentration of tensile stresses on the surface and the increase in the modulus of σ_θ until the material fractures. Also, from a mechanical point of view, it is important to note that after compression, the conical sample's shape is identical to the cylindrical one, reinforcing the idea that it behaves like a pre-bulged cylindrical sample [37].

3.6 Analysis of surface cracks

Figure 14 displays the test specimens before and after the compression tests, highlighting the surface cracks resulting from the experiments. A macroscopic examination of the appearance of the surface cracks revealed that all cylindrical samples exhibited cracks at a 45° angle from the surface, regardless of the lubrication condition and

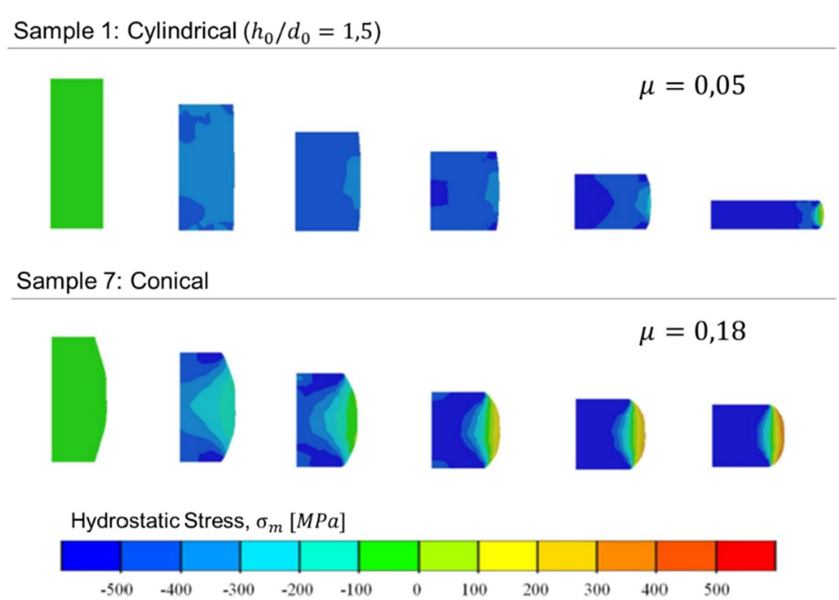

Fig. 13 Variation in hydrostatic tension during compression tests

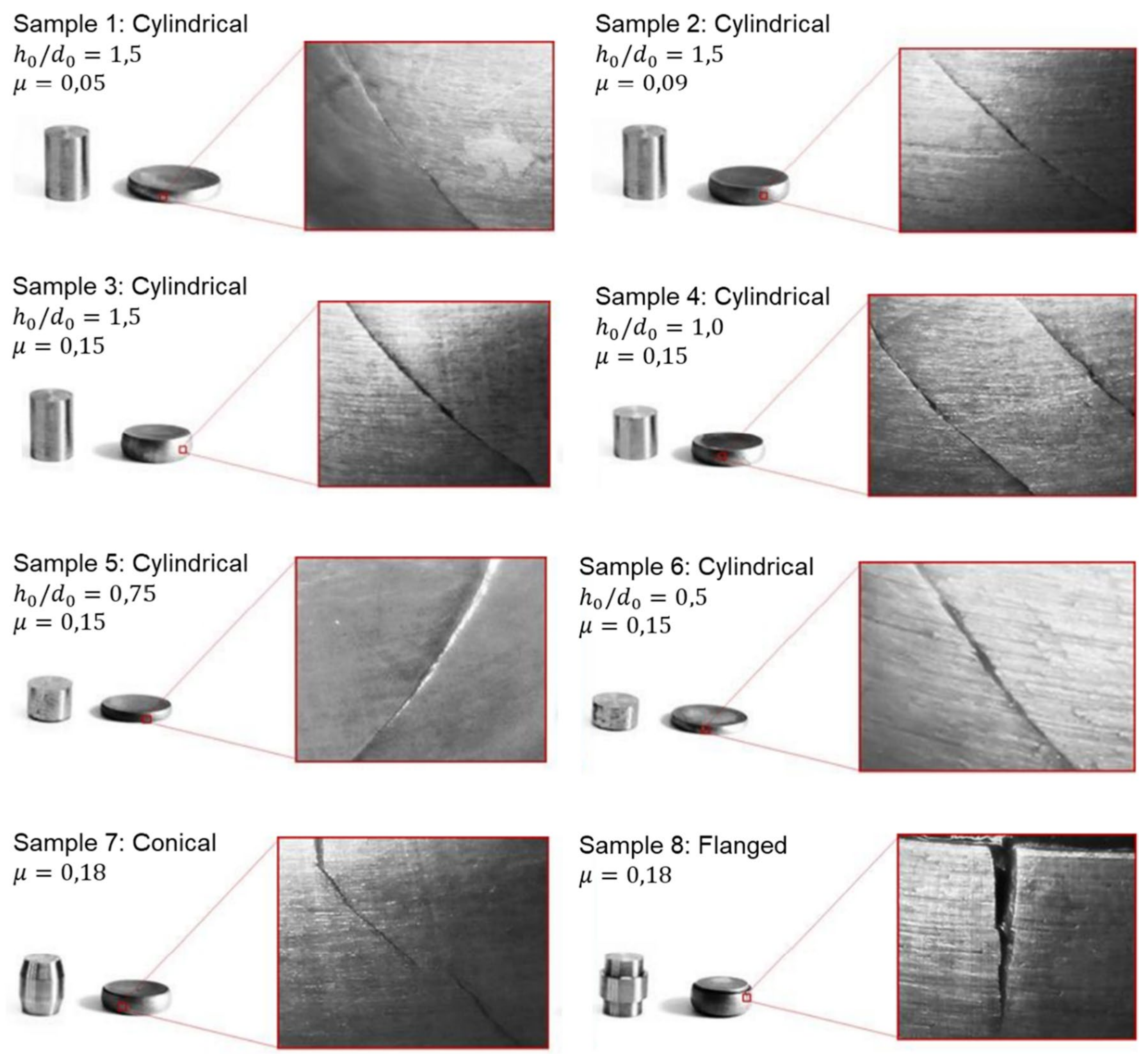

Fig. 14 Compression samples after testing

the h_0/d_0 ratio. The conical sample showed mixed cracks that propagated longitudinally near the surface and became oblique near the center of the sample. The flanged sample, on the other hand, exhibited longitudinal cracks.

In compression tests and cold forging operations, the way surface cracks propagate fundamentally depends on the friction conditions at the workpiece-tool interface and the initial geometry of the sample [42]. Despite the change in friction conditions and the h_0/d_0 ratio not affecting the way cracks formed, the pre-buckling of the samples was able to change the type of crack for the conical and flanged samples.

Researchers [43] correlated the mode of surface fracture with the stresses developed on the surface of samples subjected to compression. According to the study, longitudinal cracks form when, at the time of fracture, the axial stress on the surface of the workpiece is compressive, while oblique cracks occur when the axial stress is tensile at the time of fracture.

Observing the stress components shown in Fig. 12, it is possible to verify that, at the time of fracture, the axial stress components of the cylindrical and conical samples are compressive, while that of the flanged sample is tensile. Thus, the appearance of the cracks found in the cylindrical and flanged samples is in accordance with the result found by [43]. In the conical sample, despite the axial stress remaining negative, at the time of fracture, the magnitude of the stress component was very low. It is believed that this is the reason for the occurrence of mixed fracture.

3.7 Fracture-forming limit diagram of DIN 30MnVS6

The combination of the values of the principal deformations at the time of fracture establishes the forming limit line shown in Fig. 15. The forming limit line of the microalloyed steel DIN 30MnVS6 had a slope of − 0.5128, deviating slightly from homogeneous deformation. Thus, the line

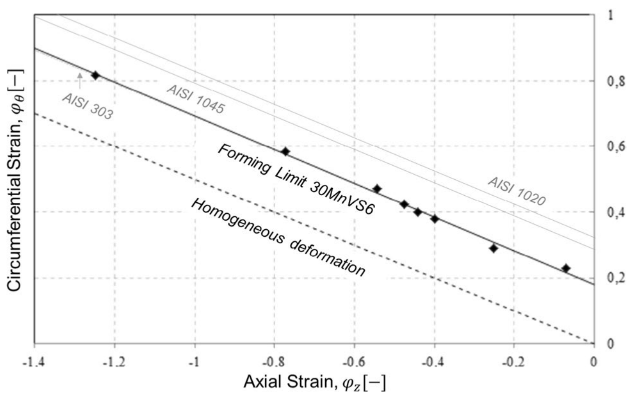

Fig. 15 Fracture-forming limit diagram of DIN 30MnVS6

that establishes the material's deformability limit can be expressed by the following equation:

$$\varphi_{\theta f} = 0.18 - 0.5128\varphi_{zf} \tag{12}$$

where $\varphi_{\theta f}$ and φ_{zf} are, respectively, the circumferential and axial deformations at fracture. The value of 0.18 corresponds to the intersection of the line on the ordinate. Since the formability limit line has a slope of approximately – 0.5 for most metals, it is the intersection value with the ordinate that defines the extent of the safe processing region on the diagram and, consequently, the formability of the material.

The intercept value of the forming limit line on the ordinate axis for DIN 30MnVS6 was 0.18. This value is considerably lower than that of other common steels, such as AISI 1045 (0.29) and AISI 1020 (0.32) [12]. These steels are known for their good ductility and are widely used in cold forging operations [2]. However, the value of 0.18 is the same as that found for the stainless steel AISI 303 [12]. AISI 303 is commonly used in cold forging processes, especially in the production of fasteners, and is known for its good formability [44]. This result reveals that the safe processing regions (below the forming limit line) of DIN 30MnVS6 and AISI 303 are identical. In processes where formability is limited by the occurrence of surface fracture, the formability of the two materials is comparable, demonstrating the suitability of the microalloyed steel DIN 30MnVS6 for application in cold forging operations.

4 Conclusions

The possibility of eliminating heat treatments used in the conventional production route of high-strength cold-forged components drives the use of steels different from those traditionally employed in the process. However, the application of a material in cold forging operations fundamentally depends on a prior analysis of formability. This research aimed to analyze the formability of microalloyed steel DIN 30MnVS6 by constructing the fracture-forming limit diagram.

Compression tests were used in the construction of the fracture-forming limit diagram of DIN 30MnVS6. In addition to defining the material's formability limit, the experimental and numerical analysis allowed an understanding of how process parameters affect formability. The tests were conducted under conditions that allowed neglecting the effects of temperature and deformation speed. Thus, stress and strain histories during plastic deformation were influenced by friction and sample geometry. It was shown that these factors, if not controlled, can significantly reduce the level of deformation the material undergoes before fracture.

The formability limit of DIN 30MnVS6 is expressed by a line, approximately parallel to the homogeneous deformation path. The intercept value of this line with the ordinate axis of the fracture-forming limit diagram can be used to quantify the material's formability. The value of 0.18 found for DIN 30MnVS6 is identical to stainless steel AISI 303, commonly used in cold forging operations.

In conclusion, microalloyed vanadium steel DIN 30MnVS6 exhibits satisfactory cold formability. The results of this study not only validate the application of this microalloyed steel in cold forging operations but can also guide the process design. The presented formability limits can be reliably used to determine whether a cold forging operation can be performed with DIN 30MnVS6 without the occurrence of defects.

Acknowledgements The authors thank CNPq, CAPES, and FAPERGS for the financial support (FAPERGS/CAPES 06/2018, process: 19/2551-0000710-8; CNPq/MCTI/FNDCT nº 18/2021, process: 404196/2021-7; CNPq research productivity – PQ1-4/2021; PDJ – 25/2021 150252/2022-6; GD – 2019; CAPES PROEXIES-2020) and the Metalforming Laboratory (LdTM) for the technical support.

Declarations

Conflict of interest The authors declare no competing interests.

References

1. Hexa Research (2019) Cold forged products market size and forecast, by material (stainless steel, aluminium, copper), by application (industrial, aerospace, automotive, building & construction, consumer goods) and segment forecast, 2015 – 2025 [Online] Available: https://www.hexaresearch.com/research-report/cold-forged-products-market
2. International Cold Forging Group (2007) Document No.18/07, 40 Years History Document
3. Liewald M, Kannewurf M, Industrieverband Massivumformung (2012) Kaltmassivumformung: Präzision in groben Serien, Info-Reihe Massivumformung. Extraausgabe
4. Hasler S, Roelofs H, Urlau U (2011) New bainitic steel for cold heading applications. In Proceedings of the 3rd International

Conference on Steels for Cars and Trucks (SCT 2011), Salzburg, Austria
5. Sabih A, Wanjara P, Nemes J (2005) Characterization of internal voids and cracks in cold heading of dual phase steel. ISIJ Int 45(8):1179–1186
6. Kim SJ, Lee T, Hwang J-K (2020) High-strength bolt manufactured by an extrusion-based forming process using twinning-induced plasticity steel. J Manuf Process 59:33–42
7. Li Z, Wu D (2007) Study of the high strength and low yield ratio cold forging steel. Mater Sci Eng: A 452–453:142–148
8. Krauss G, Microstructures, Processing, and Properties of Steels, Metal Handbook (1990). Properties and selection: Irons steels and high performance alloys, vol 1. ASM International, Handbook Committee
9. Matlock D, Speer J (2009) Microalloying concepts and application in long products. Mater Sci Technol 25(9):1118–1125
10. Dieter GE, Kuhn HA, Semiatin SL (eds) (2003) Handbook of formability and process design. ASM International
11. Thomason PF (1969) Tensile plastic instability and ductile fracture criteria in uniaxial compression tests. Int J Mech Sci 11(2):187–198
12. Kuhn HA, Lee PW (1971) Strain instability and fracture at the surface of upset cylinders. Metals Trans 2(11):3197–3202
13. Kudo H, Sato K, Aoi EK (1968) On cold forgability test. CIRP Ann 16:309–18
14. Shah DC (1974) Use of metallic materials to model the flow and fracture of steel in cold upsetting. In: Marcantonio A (ed) Mechanical Working and Steel Processing XIV (Dalton, IL), 23–24 Jan 1974. AIME, pp 285–300
15. Levy BS, Fine TE (1973) Effect of composition and process variables on deformation in simple upsetting. Mechanical Working and Steel Processing VI. The Iron and Steel Society of AIME, New York, NY
16. Thomason PF (1968) The use of pure aluminum as an analogue for the history of plastic flow. Studies of Ductile Fracture Criteria in Steel Compression Specimens. Int J Mech Sci 10(6):501–518
17. Lee PW, Kuhn HA (1972) Fracture in cold upset forging - a criterion and model. Metall Trans 4:969–74
18. Woodall SM, Schey JA (1978) Determination of ductility for bulk deformation, Formability Topics — Metallic Materials, ASTM STP 647. In: Niemeier BA, Schmeider AK, Newby JR (eds) American Society for Testing and Materials. pp 191–205. https://doi.org/10.1520/STP30053S
19. Oh SI, Kobayashi S (1976) Formability of aluminum alloy 7075–T6 in upsetting and rolling. J Eng Ind (Trans. ASME) 98(3):800–806
20. Bariani P (1984) Cold formability limits of 1100 aluminum, 2024 and 7075 aluminum alloys in isothermal and adiabatic upsetting tests. Adv Technol Plast 11:857–65
21. Shah J, Kuhn HA (1986) An empirical formula for formability limits in cold upsetting and bolt heading. J Appl Metalwork 4(3):255–61
22. Erman E, Kuhn HA, Fitzsimons G (1983) Novel test specimens for formability testing. In compression testing of homogeneous materials and composites. ASTM International, pp 279–291
23. Kiviruori S, Sulonen M (1978) Formability limits and fracturing modes of uniaxial compression specimens. CIRP Ann 27(1):141–145
24. Sornberger G, Ramparany F, Cerles JM, Teirlinck D (1986) Ductility of a continuous cast 5056 aluminum alloy rod. Formability and Metallurgical Structure, Proc. Symp., Mechanical Metallurgy and Shaping and Forming Committees of TMS, AIME (Orlando, FL), 5–9 Oct 1986, pp 327–340
25. Thomason PF (1969) The free surface ductility of uniaxial compression specimens with longitudinal surface defects. Int J Mech Sci 11(1):65–73
26. Mayagawa M, Shinohara M, Asao H (1971) Compression test of cylinders with longitudinal notches for comparison of cold upset – forgeability. J Jpn Soc Technol Plast 12(122):183
27. Fukuda T, Hajita H (1975) Effect of longitudinal surface defect on the steel wire on upsetting limits. J Jpn Soc Technol Plast 16(170):255–263
28. Fan Z (1995) The grain size dependence of ductile fracture toughness of polycrystalline metals and alloys. Mater Sci Eng 191(1–2):73–83
29. El-Domiaty A, Shaker M (1991) A note on the formability of porous steel preforms. J Mater Process Technol 25(2):229–33
30. Clift SE, Hartley P, Sturgess CEN, Rowe GW (1990) Fracture prediction in plastic deformation processes. Int J Mech Sci 32(1):1–7
31. Zhu YY, Cescotto S, Habraken AM (1992) A fully coupled elasticplastic damage modeling and fracture criteria in metal forming processes. J Mater Process Technol 32(1–2):197–204
32. Wifi AS, El-Monayri AH, El-Abassi N (1992) Finite element determination of formability limits for disks and rings under different upsetting conditions. Adv Mater Process Technol 56(1–4):918–32
33. Shabara MA, El-Domiaty AA, Kandil A (1996) Validity assessment of ductile fracture criteria in cold forming. J Mater Eng Perform 5:478–88
34. European Standards, BS EN (1998) 10267–1998 Ferritic-pearlitic steels for precipitation hardening from hotworking temperatures
35. Hawkyard JB, Johnson W (1967) An analysis of the changes in geometry of short hollow cylinder during axial compression. Pergamon Press Ltd, Int. J. Mech. Sci
36. Bao Y (2003) Prediction of ductile crack formation in uncracked bodies, engineering mechanics. PhD Thesis, Massachusetts Institute of Technology
37. Landre J (2003) On the utilisation of ductile fracture criteria in cold forging. Finite Elem Anal Des 39:175–186
38. Karlsson B, Lindén G (1975) Plastic deformation of ferrite - pearlite structures in steel. Mater Sci Eng 17(2):209–19
39. Jenner A, Bradley D (1981) Cold upsetting and free surface ductility. J Mech Work Technol 5(1–2):31–43
40. Rao JB, Kamluddin S, Rao JA, Sarcar MMM, Bhargava NRMR (2009) Deformation behavior of Al-4Cu-2Mg alloy during cold upset forging. J Alloy Compd 471(1–2):128–136
41. Gouveia BPPA, Rodrigues JMC, Martins PAF (2000) Ductile fracture in metalworking: experimental and theoretical research. J Mater Process Technol 101(1–3):52–63
42. Yanshan L, Whan IJ, Hoon H, Qi C, Jung-Han S (October 2018) Correlation of the maximum shear stress with micro-mechanisms of ductile fracture for metals with high strength-to-weight ratio. Int J Mech Sci, Vol 146–147:583–601
43. Kudo H, Aoi K (1967) Effect of compression test condition upon fracturing of a medium carbon steel. J Jpn Soc Technol Plast 8(72):17–27
44. Nickel Institute (2019) Cold forming stainless steel bar and wire. A designers' handbook series, n° 9019. American Iron and Steel Institute. [Online] Available: https://www.nickelinstitute.org/media/4666/ni_aisi_9019_coldforming.pdf